Theory of the anisotropy of the electron Hall mobility in *n*-type 4H– and 6H–SiC

Hisaomi Iwata and Kohei M. Itoh[a)]
Department of Applied Physics and Physico-Informatics, Keio University, Yokohama 223-8522, Japan

Gerhard Pensl
Institut für Angewandte Physik, Universität Erlangen–Nümberg, D-91058 Erlangen, Germany

(Received 14 February 2000; accepted for publication 5 May 2000)

A theoretical model for the calculation of the anisotropy in the electron Hall mobility is reported for *n*-type bulk single crystals of 4H– and 6H–SiC for the three distinct Hall measurement configurations: (a) [$\mathbf{B}\|\mathbf{c}$, $\mathbf{j}\perp\mathbf{c}$], (b) [$\mathbf{B}\perp\mathbf{c}$, $\mathbf{j}\perp\mathbf{c}$], and (c) [$\mathbf{B}\perp\mathbf{c}$, $\mathbf{j}\|\mathbf{c}$], where **B**, **j**, and **c** are the directions of the magnetic field, current flow, and *c* axis of the hexagonal unit cell, respectively. Comparison with experimental results shows that the anisotropy of the electron transport in both 4H– and 6H–SiC can be explained solely by the anisotropy in the effective electron mass tensors.
 [S0021-8979(00)01316-5]

I. INTRODUCTION

The electron mobility of 4H– and 6H–SiC as determined by the Hall effect, i.e., the electron Hall mobility, depends strongly on the geometrical configurations of the Hall measurement due to the anisotropic structure of the conduction bands.[1,2] Quantitative understanding of the anisotropy of the electron transport in 4H– and 6H–SiC is important for designing SiC-based devices and reliable device simulators. Although several growth- and characterization-related studies on 4H– and 6H–SiC have recently been reported,[3,4] the number of theoretical studies on electron transport is rather limited.[5–12] Moreover, most of the transport studies are based on Monte Carlo simulations in which the effect of the externally applied magnetic field cannot be included, i.e., the direct comparison of Monte Carlo results with the experimentally determined Hall mobility is not possible.[5–9] In order to improve this situation, we have recently reported analytical expressions for the electron mobility of 6H–SiC taking into account the magnetic field for the three distinct Hall measurement configurations shown in Fig. 1: (a) [$\mathbf{B}\|\mathbf{c}$, $\mathbf{j}\perp\mathbf{c}$], (b) [$\mathbf{B}\perp\mathbf{c}$, $\mathbf{j}\perp\mathbf{c}$], and (c) [$\mathbf{B}\perp\mathbf{c}$, $\mathbf{j}\|\mathbf{c}$], where **B**, **j**, and **c** are the directions of the magnetic field, current flow, and *c* axis of the hexagonal unit cell, respectively.[11] This analytical calculation of the Hall mobility provides the possibility to directly compare theoretical results with the experimentally determined electron Hall mobilities.[11]

In this article, we extend our previous work on 6H–SiC to the 4H–SiC polytype, and compare the theoretically obtained electron Hall mobilities with the experimental values determined for the three distinct configurations shown in Figs. 1(a)–1(c). The theory reported in Ref. 11 has further been refined, i.e., we shall repeat similar calculations for 6H–SiC already reported in Ref. 11 using the improved model described in the next section. It is the main purpose of this work to demonstrate that the anisotropy of the electron Hall mobility for both the 4H– and 6H–SiC polytype is solely dominated by the anisotropy of the effective electron mass tensors.

II. METHOD AND MODEL

Our model is based on the conduction-band structure determined recently by first-principle calculations and experiments.[13–18] We assume that there are six semiellipsoidal and parabolic constant energy surfaces centered exactly at *M* points in the first Brillouin zone for both 4H– and 6H–SiC, as shown in Figs. 2(a) and 2(b), respectively. This assumption is reasonable since the Hall effect is a typical low-field transport that takes place at the bottom of the conduction band where parabolic approximation is valid. The effective masses in the *M*-Γ, *M*-*K*, and *M*-*L* directions in the reciprocal space of the hexagonal unit cell are listed in Table I. Our strategy for obtaining the Hall mobility consists of the following steps. First, we derive an expression of the conductivity tensor including the magnetic field for one ellipsoid from the semiclassical Boltzmann transport equation using the relaxation time approximation and Maxwellian approximation. Then, we place three ellipsoids in proper positions in the reciprocal space by 120° rotation around the *c* axis. Finally, we obtain the total conductivity tensor by adding the

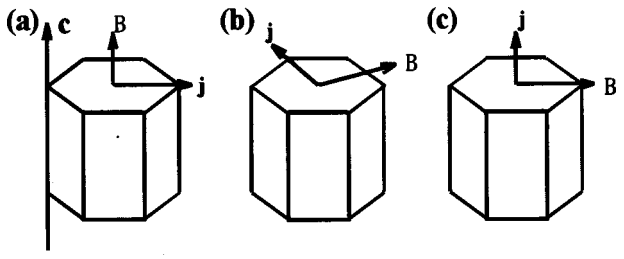

FIG. 1. Schematic diagram of the three distinct Hall measurement configurations: (a) [$\mathbf{B}\|\mathbf{c}$, $\mathbf{j}\perp\mathbf{c}$], (b) [$\mathbf{B}\perp\mathbf{c}$, $\mathbf{j}\perp\mathbf{c}$], and (c) [$\mathbf{B}\perp\mathbf{c}$, $\mathbf{j}\|\mathbf{c}$].

a)Electronic mail: kitoh@appi.keio.ac.jp

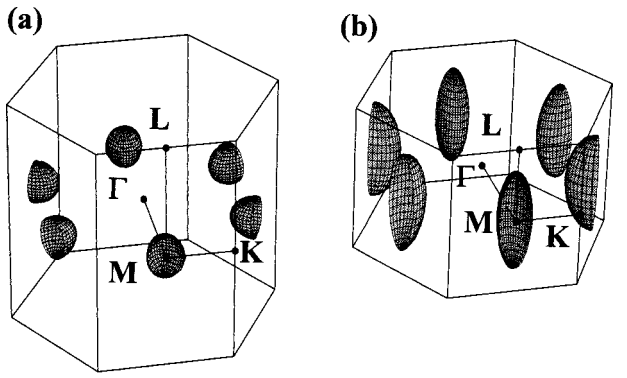

FIG. 2. Constant energy surfaces for (a) 4H–SiC and (b) 6H–SiC in the first Brillouin zone.

contributions from each of the three ellipsoids. This procedure leads to analytical expressions for the drift and Hall mobility as a function of the average electron momentum relaxation time and the effective masses.

For one ellipsoid shown in Fig. 3, the electric current density vector $\mathbf{J}'$ in the presence of the magnetic field is derived from the Boltzmann transport equation using the relaxation time approximation and Maxwellian approximation:

$$\mathbf{J}'=\boldsymbol{\sigma}'\mathbf{E}'=\begin{pmatrix}\sigma'_{11} & -\sigma'_{12}B'_3 & \sigma'_{31}B'_2\\ \sigma'_{21}B'_3 & \sigma'_{22} & -\sigma'_{23}B'_1\\ -\sigma'_{31}B'_2 & \sigma'_{32}B'_1 & \sigma'_{33}\end{pmatrix}\mathbf{E}', \quad (1)$$

where

$$\sigma'_{ii}=qn'\frac{q}{m_i^*}\frac{\int_0^\infty dx\int_0^{2\pi}d\varphi\int_0^{\pi}\tau_{\mathbf{k}}x^{3/2}\exp(-x)h_i\sin\theta d\theta}{\int_0^\infty dx\int_0^{2\pi}d\varphi\int_0^{\pi}x^{3/2}\exp(-x)h_i\sin\theta d\theta}$$

$$=qn'\frac{q}{m_i^*}\langle\tau_{\mathbf{k}}\rangle_i, \quad (2a)$$

$$\sigma'_{ij}=qn'\frac{q^2}{m_i^*m_j^*}\frac{\int_0^\infty dx\int_0^{2\pi}d\varphi\int_0^{\pi}\tau_{\mathbf{k}}^2x^{3/2}\exp(-x)h_i\sin\theta d\theta}{\int_0^\infty dx\int_0^{2\pi}d\varphi\int_0^{\pi}x^{3/2}\exp(-x)h_i\sin\theta d\theta}$$

$$=qn'\frac{q^2}{m_i^*m_j^*}\langle\tau_{\mathbf{k}}^2\rangle_i, \quad (2b)$$

TABLE I. Effective masses of 4H– and 6H–SiC.

	4H–SiC[m_0]	6H–SiC[m_0]
$m_{M\text{-}\Gamma}$	0.57	0.75
$m_{M\text{-}K}$	0.28	0.24
$m_{M\text{-}L}$	0.31	1.83

and

$$n'=2\left(\frac{m^*_{\text{d.s.}}k_BT}{2\pi\hbar^2}\right)^{3/2}\exp\{-(E_C-E_F)/k_BT\}, \quad (3)$$

$$x=\frac{\varepsilon}{k_BT}, \quad (4)$$

$$h_1=\frac{m_1^*v_1^2}{2\varepsilon}=\cos^2\varphi\sin^2\theta, \quad (5a)$$

$$h_2=\frac{m_2^*v_2^2}{2\varepsilon}=\sin^2\varphi\sin^2\theta, \quad (5b)$$

$$h_3=\frac{m_3^*v_3^2}{2\varepsilon}=\cos^2\theta. \quad (5c)$$

$\mathbf{E}'$ is the applied electric-field vector for one ellipsoid, q is the electron charge, k_B is the Boltzmann constant, T is the temperature, $\tau_{\mathbf{k}}$ is the electron momentum relaxation time for an electron having wave vector $\mathbf{k}$, ε is the kinetic energy of the electron, $B'_{i=1,2,3}$ is the ith component of the applied magnetic field for one ellipsoid, $m^*_{i,j=1,2,3}$ is the ith component of the effective mass, and $v_{i=1,2,3}$ is the ith component of the electron velocity. The subscripts $i,j=1,2,3$ correspond to x, y, and z directions for one ellipsoid shown in Fig. 3 taken along the M-Γ, M-K, and M-L directions, respectively. n' is the electron concentration in each ellipsoid, where $m^*_{\text{d.s.}}$ is the density of states effective mass, E_C is the energy of the conduction-band minima, and E_F is Fermi level.

Three ellipsoids are placed in the proper positions and combined into the total conductivity tensor by adding the contributions from each ellipsoid. The total conductivity tensor is given by

$$\mathbf{J}=\sigma\mathbf{E}=\frac{3}{2}\begin{bmatrix}\sigma'_{11}+\sigma'_{22} & -(\sigma'_{12}+\sigma'_{21})B_3 & (\sigma'_{13}+\sigma'_{23})B_2\\ (\sigma'_{12}+\sigma'_{21})B_3 & \sigma'_{11}+\sigma'_{22} & -(\sigma'_{13}+\sigma'_{23})B_1\\ -(\sigma'_{31}+\sigma'_{32})B_2 & (\sigma'_{31}+\sigma'_{32})B_1 & 2\sigma'_{33}\end{bmatrix}\mathbf{E}. \quad (6)$$

$\mathbf{E}$ and $\mathbf{B}$ are the electric-field vector and the magnetic-field vector applied to a sample, respectively.

This expression allows us to calculate both the electron drift and Hall mobility for arbitrary crystallographic directions. For the three Hall measurement configurations (a) [$\mathbf{B}\|\mathbf{c}$, $\mathbf{j}\perp\mathbf{c}$], (b) [$\mathbf{B}\perp\mathbf{c}$, $\mathbf{j}\perp\mathbf{c}$], and (c) [$\mathbf{B}\perp\mathbf{c}$, $\mathbf{j}\|\mathbf{c}$] shown in Fig. 1, we obtain the following expressions for the electron Hall mobility $\mu_{H(a)}$, $\mu_{H(b)}$, and $\mu_{H(c)}$, respectively,[1]

$$\mu_{H(a)}=\frac{\sigma'_{12}+\sigma'_{21}}{\sigma'_{11}+\sigma'_{22}}=q\frac{\langle\tau_{\mathbf{k}}^2\rangle_1+\langle\tau_{\mathbf{k}}^2\rangle_2}{m_1^*\langle\tau_{\mathbf{k}}\rangle_2+m_2^*\langle\tau_{\mathbf{k}}\rangle_1}, \quad (7a)$$

$$\mu_{H(b)}=\frac{\sigma'_{31}+\sigma'_{32}}{2\sigma'_{33}}=\frac{q}{2}\left(\frac{\langle\tau_{\mathbf{k}}^2\rangle_3}{m_1^*\langle\tau_{\mathbf{k}}\rangle_3}+\frac{\langle\tau_{\mathbf{k}}^2\rangle_3}{m_2^*\langle\tau_{\mathbf{k}}\rangle_3}\right), \quad (7b)$$

$$\mu_{H(c)}=\frac{\sigma'_{13}+\sigma'_{23}}{\sigma'_{11}+\sigma'_{22}}=q\frac{m_1^*\langle\tau_{\mathbf{k}}^2\rangle_2+m_2^*\langle\tau_{\mathbf{k}}^2\rangle_1}{m_1^*m_3^*\langle\tau_{\mathbf{k}}\rangle_2+m_2^*m_3^*\langle\tau_{\mathbf{k}}\rangle_1}. \quad (7c)$$

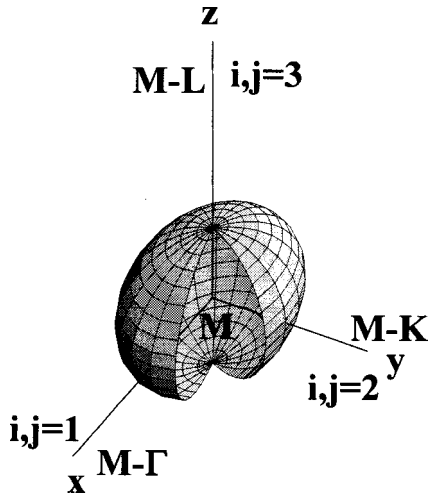

FIG. 3. Coordinate system employed for one ellipsoidal constant energy surface in reciprocal space.

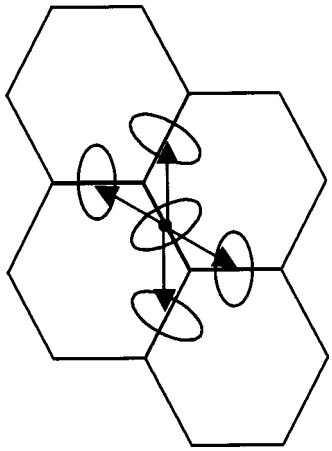

FIG. 4. Top view of the Brillouin zone showing electron transition by intervalley scattering for 4H– and 6H–SiC.

Equations 7(a)–7(c) are functions of the effective masses and the average momentum relaxation time. Since the effective mass tensors have already been obtained by the recent first-principle calculations and the experiments,[13–18] we need to determine the values of $\langle \tau_{\mathbf{k}} \rangle_{1-3}$ and $\langle \tau_{\mathbf{k}}^2 \rangle_{1-3}$ in order to calculate the electron Hall mobility.

The following four scattering mechanisms are considered for the calculation of relaxation times: ionized impurity scattering, acoustic phonon deformation potential scattering, polar optical phonon scattering, and intervalley phonon deformation potential scattering. We consider the effect of ellipsoidal constant energy surfaces on the ionized impurity scattering because it is the most sensitive to the band-structure anisotropy among the four scattering mechanisms. The scattering rate for ionized impurity scattering τ_{ion}^{-1} is given by[19–21]

$$\tau_{\mathrm{ion}}^{-1}=\frac{1}{(2\pi)^3}\frac{2\pi}{\hbar}\frac{\sqrt{2m_1^* m_2^* m_3^*}}{\hbar^3}\sqrt{xk_BT}\times\int_0^{2\pi}d\varphi'\int_0^{\pi}\frac{n_{\mathrm{ion}}q^4}{\kappa_S^2\varepsilon_0^2}\left(\frac{1}{|\mathbf{k}-\mathbf{k}'|^2+L_D^{-2}}\right)^2\times\left(1-\frac{\mathbf{v}\cdot\mathbf{v}'}{\mathbf{v}^2}\right)\sin\theta'\,d\theta', \tag{8}$$

where $\mathbf{v}$ and $\mathbf{v}'$ are the velocity of incident and scattered electrons having wave vectors $\mathbf{k}$ and $\mathbf{k}'$, respectively, n_{ion} is the concentration of ionized impurities, κ_S is the static relative dielectric constant, ε_0 is the dielectric constant in vacuum, and L_D is the screening length. The calculation of L_D is performed using a model developed for compensated semiconductors by Falicov and Cuevas,[22,23] since the theory is compared with the experimental data taken on relatively compensated 4H– and 6H–SiC samples. In this case, the Falicov and Cuevas model is more appropriate than the standard Brooks and Herring model.[24] The screening length L_D is given by[23]

$$L_D=[8\pi(N_{\mathrm{MJ}}-N_{\mathrm{MN}})]^{-1/3}, \tag{9}$$

where N_{MJ} and N_{MN} are concentrations of the majority and minority impurities, respectively.

The scattering rate for acoustic phonon deformation potential scattering τ_{ac}^{-1} is given by[20,21,25]

$$\tau_{\mathrm{ac}}^{-1}=\frac{\sqrt{2}(k_BTm_{\mathrm{d.s.}}^*)^{2/3}D_{\mathrm{ac}}^2}{\pi\hbar^4\rho v_s^2}x^{1/2}, \tag{10}$$

where D_{ac} is the acoustic deformation potential, ρ is the density, and v_s is the sound velocity in a particular semiconductor.

The scattering rate for polar optical phonon scattering τ_{pop}^{-1} is given by[20,21,26]

$$\tau_{\mathrm{pop}}^{-1}=\frac{q^2\omega_p(\kappa_S/\kappa_\infty-1)}{4\pi\kappa_S\varepsilon_0\hbar\sqrt{2xk_BT/m_{\mathrm{d.s.}}^*}}\Bigg[n(\omega_p)(1+\hbar\omega_p/xk_BT)^{1/2}+\{n(\omega_p)+1\}\mathrm{Re}(1-\hbar\omega_p/xk_BT)^{1/2}-\frac{\hbar\omega_p n(\omega_p)}{xk_BT}\times\sinh^{-1}(xk_BT/\hbar\omega_p)^{1/2}+\frac{\hbar\omega_p\{n(\omega_p)+1\}}{xk_BT}\times\sinh^{-1}(\mathrm{Re}(xk_BT/\hbar\omega_p-1))^{1/2}\Bigg], \tag{11}$$

where $n(\omega)=1/\{\exp(\hbar\omega/k_BT)-1\}$ is the Bose–Einstein distribution function, κ_∞ is the optical relative dielectric constant, and $\hbar\omega_p$ is the polar optical phonon energy.

The scattering rate for intervalley phonon deformation potential scattering τ_{int}^{-1} is given by[20,21,27]

$$\tau_{\mathrm{int}}^{-1}=\frac{ZD_{\mathrm{int}}m_{\mathrm{d.s.}}^{*\,3/2}}{\sqrt{2}\pi\hbar^3\omega_{\mathrm{int}}\rho}[n(\omega_{\mathrm{int}})(xk_BT+\hbar\omega_{\mathrm{int}})^{1/2}+\{n(\omega_{\mathrm{int}})+1\}\mathrm{Re}(xk_BT-\hbar\omega_{\mathrm{int}})^{1/2}], \tag{12}$$

where $\hbar\omega_{\mathrm{int}}$ is the energy of the intervalley phonon, D_{int} is the intervalley phonon deformation potential, and $Z=4$ is the number of final valleys available for intervalley scattering, as shown in Fig. 4.

Finally, we obtain the average momentum relaxation time by

$$\langle \tau_{\mathbf{k}} \rangle_i = \frac{\int_0^\infty dx \int_0^{2\pi} d\varphi \int_0^\pi \left(\frac{1}{\tau_{\text{ion}}^{-1} + \tau_{\text{ac}}^{-1} + \tau_{\text{op}}^{-1} + \tau_{\text{int}}^{-1}} \right) x^{3/2} \exp(-x) h_i \sin\theta d\theta}{\int_0^\infty dx \int_0^{2\pi} d\varphi \int_0^\pi x^{3/2} \exp(-x) h_i \sin\theta d\theta}, \tag{13a}$$

$$\langle \tau_{\mathbf{k}}^2 \rangle_i = \frac{\int_0^\infty dx \int_0^{2\pi} d\varphi \int_0^\pi \left(\frac{1}{\tau_{\text{ion}}^{-1} + \tau_{\text{ac}}^{-1} + \tau_{\text{op}}^{-1} + \tau_{\text{int}}^{-1}} \right)^2 x^{3/2} \exp(-x) h_i \sin\theta d\theta}{\int_0^\infty dx \int_0^{2\pi} d\varphi \int_0^\pi x^{3/2} \exp(-x) h_i \sin\theta d\theta}. \tag{13b}$$

The values of the parameters, ε_0, κ_∞, ρ, v_s, D_{ac}, $\hbar\omega_p$, D_{int}, and $\hbar\omega_{\text{int}}$ are given in Table II, and D_{ac} and D_{int} apply only to the bulk 4H– and 6H–SiC employed in this study. For example, we should note that the value of $D_{\text{ac}} \approx 21$ eV is significantly different from $D_{\text{ac}} \approx 11$ eV obtained from much higher crystalline quality, chemical-vapor-deposited (CVD) 4H– and 6H–SiC thin films.[12,28,29] In general, the crystalline quality of bulk 4H– and 6H–SiC is much worse than that of CVD grown thin films. However, the electron Hall mobility measurement for the three distinct configurations shown in Figs. 1(a)–1(c) cannot be realized on one and the same sample using a thin film, i.e., we are forced for this work to employ the electron Hall mobility data taken on bulk samples. It has theoretically been shown that the correlated distribution of defects and impurities in semiconductors leads to a lowering of the carrier mobility with little change in its temperature dependence.[30] Scattering by point defects, dislocations, and micropipes leads to a further lowering of the mobility with the temperature dependence $\propto T^{-p}$, where $p = 0 - \frac{3}{2}$.[31,32] The simplest way to incorporate such an effect for the mobility calculation of bulk 4H– and 6H–SiC, in which inhomogeneous distribution of structural defects is likely to be present, is by adjusting the values of D_{ac} and D_{int} for a particular sample, i.e., the values of D_{ac} and D_{int} listed in Table II are obtained by a numerical fit of the experimental data for 4H– and 6H–SiC samples. The values of $\hbar\omega_p$ and $\hbar\omega_{\text{int}}$ are taken from Ref. 8. The purpose of the present study is to demonstrate that the anisotropy of the electron Hall mobility in 4H– and 6H–SiC is determined solely by the corresponding anisotropic effective mass tensors. We can achieve this goal as long as we employ the same set of the parameters for the three Hall-effect configurations shown in Figs. 1(a)–1(c) and check whether the relative change in the Hall mobility between the three configurations agrees with the experimental results.

III. RESULTS AND DISCUSSION

Figures 5(a)–5(f) show the comparison of our Hall mobility calculations using Eqs. (7a)–(7c) (solid curves) with the experimental Hall-effect data (filled circles) in the three distinct configurations for 4H– and 6H–SiC. The experimental data are the same as the ones shown in Ref. 10. The donor (nitrogen) and acceptor concentration for the 4H–SiC sample are 6.4×10^{18} and $3.6\times10^{18}\,\text{cm}^{-3}$, respectively, while those for 6H–SiC are 3.5×10^{16} and $1.1\times10^{16}\,\text{cm}^{-3}$, respectively. The contribution of various scattering mechanisms to the total electron Hall mobility is also shown. Comparison between Figs. 5(a) and 5(c) for the 4H–SiC and between Figs. 5(d) and 5(f) for the 6H–SiC shows that the relative change of the experimentally determined Hall mobility between the three configurations is reproduced accurately by our theory. Since the effect of anisotropy is described by the difference between m_1^*, m_2^*, and m_3^* in Eqs. (7a)–(7c) we conclude that the anisotropy of the electron Hall mobility is described solely by the anisotropy of the effective mass tensors.

For 6H–SiC, the electron Hall mobility values in configuration (b) [$\mathbf{B}\perp\mathbf{c}$, $\mathbf{j}\perp\mathbf{c}$] are the largest throughout the temperature range shown, while the corresponding values in configuration (c) [$\mathbf{B}\perp\mathbf{c}$, $\mathbf{j}\parallel\mathbf{c}$] are the smallest. The maximum anisotropy factor $\mu[\mathbf{B}\perp\mathbf{c}, \mathbf{j}\perp\mathbf{c}]/\mu[\mathbf{B}\perp\mathbf{c}, \mathbf{j}\parallel\mathbf{c}]$ is about 5. For 4H–SiC, the electron Hall mobility values in configuration (c) [$\mathbf{B}\perp\mathbf{c}$, $\mathbf{j}\parallel\mathbf{c}$] are the largest while the corresponding values in configuration (a) [$\mathbf{B}\parallel\mathbf{c}$, $\mathbf{j}\perp\mathbf{c}$] are the smallest. The maximum anisotropy factor $\mu[\mathbf{B}\parallel\mathbf{c}, \mathbf{j}\perp\mathbf{c}]/\mu[\mathbf{B}\perp\mathbf{c}, \mathbf{j}\parallel\mathbf{c}]$ is about 0.7. The anisotropy of the Hall mobility for 4H–SiC is relatively small in comparison to that of 6H–SiC, caused by the smaller anisotropy of the effective mass tensor for 4H–SiC compared to 6H–SiC.

The contributions of the various scattering mechanisms shown in Figs. 5(a)–5(f) indicate that the dominant scattering mechanisms in both 4H– and 6H–SiC are ionized impurity scattering, acoustic phonon scattering, and intervalley scattering, for low-, intermediate-, and high-temperature regions, respectively. The deviation between our theory and experiment at low temperatures for both 4H– and 6H–SiC is possibly due to the scattering by crystal defects such as point defects, dislocations, and micropipes, while our calculations do not incorporate such effects accurately. It is also possible that the experimentally measured mobility in the low-temperature region does not represent the mobility of free carriers due to the occurrence of hopping conduction.[33,34] The hopping conduction tends to lower the mobility while we ignore such an effect completely.

TABLE II. Parameters used for the calculation of relaxation time.

	4H–SiC	6H–SiC
Static relative dielectric constant ε_0	9.7	9.7
Optical relative dielectric constant κ_∞	6.5	6.5
Density ρ (g/cm^3)	3.166	3.166
Sound velocity v_s (10^4 m/s)	1.37	1.37
Acoustic deformation potential D_{ac} (eV)	21.0	21.5
Polor optical phonon energy $\hbar\omega_p$ (meV)	120	120
Intervalley deformation potential D_{int} (10^9 eV/cm)	3.7	2.7
Intervalley phonon energy $\hbar\omega_{\text{int}}$ (meV)	85.4	85.4

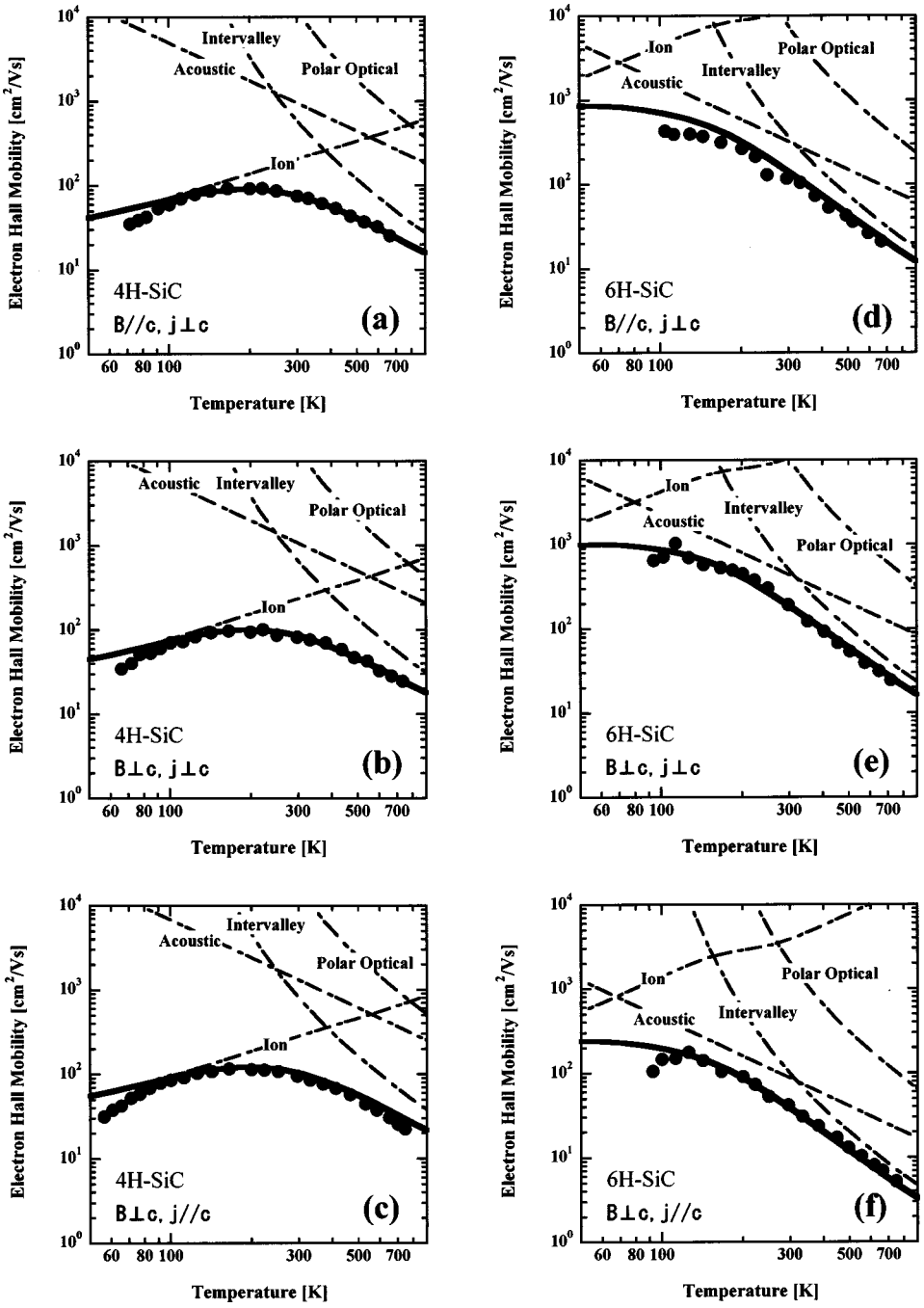

FIG. 5. Comparison of our Hall mobility calculations (solid curve) with the experimental Hall-effect data (filled circles) for; (a) 4H–SiC in the configuration given in Fig. 1(a); (b) 4H–SiC in the configuration given in Fig. 1(b); (c) 4H–SiC in the configuration given in Fig. 1(c); (d) 6H–SiC in the configuration given in Fig. 1(a); (e) 6H–SiC in the configuration given in Fig. 1(b); and (f) 6H–SiC in the configuration given in Fig. 1(c), respectively. The contribution of various scattering mechanisms to the total electron Hall mobility is shown by broken curves. Experimental data are taken from Ref. 10.

IV. CONCLUSION

We have developed a theoretical model for calculation of the electron Hall mobility in 4H– and 6H–SiC for the three distinct Hall measurement configurations. Our calculation of the electron Hall mobility for 4H– and 6H–SiC as a function of temperature has revealed that the anisotropy of the electron Hall mobility can be determined solely by the anisotropy in the effective masses. The contribution of various scattering mechanisms to the total electron Hall mobility has been shown for both 4H– and 6H–SiC. The dominant scattering mechanisms in 4H– and 6H–SiC are ionized impurity scattering, acoustic phonon scattering, and intervalley scattering, for the low-, intermediate-, and high-temperature regions, respectively.

ACKNOWLEDGMENTS

The authors would like to acknowledge T. Kinoshita, M. Schadt, E. Bellotti, and H.-E. Nilsson for fruitful discussions.

[1] M. Schadt, G. Pensl, R. P. Devaty, W. J. Choyke, R. Stein, and D. Stephani, Appl. Phys. Lett. **65**, 312 (1994).
[2] W. J. Choyke and G. Pensl, MRS Bull. **22**, 25 (1997).
[3] See, for example, a series of papers published in Phys. Status Solidi A **162** (1997).
[4] See, for example, a series of papers published in Phys. Status Solidi B **202** (1997).
[5] R. P. Joshi, J. Appl. Phys. **78**, 5518 (1995).
[6] R. P. Joshi and D. K. Ferry, Solid-State Electron. **38**, 1911 (1995).
[7] H.-E. Nilsson, U. Sannemo, and C. S. Petersson, J. Appl. Phys. **80**, 3365 (1996).
[8] R. Mickevičius and J. H. Zhao, J. Appl. Phys. **83**, 3161 (1998).

[9] H.-E. Nilsson, M. Hjelm, and C. Fröjdh, J. Appl. Phys. **86**, 965 (1999).
[10] T. Kinoshita, K. M. Itoh, J. Muto, M. Schadt, G. Pensl, and K. Takeda, Mater. Sci. Forum **264-268**, 295 (1998).
[11] T. Kinoshita, K. M. Itoh, M. Schadt, and G. Pensl, J. Appl. Phys. **85**, 8193 (1999).
[12] H. Iwata and K. M. Itoh, in Proceedings of the International Conference on Silicon Carbide and Related Materials 1999 (to be published).
[13] C. Persson and U. Lindefelt, Phys. Rev. B **54**, 10257 (1996).
[14] W. R. L. Lambrecht and B. Segall, Phys. Rev. B **54**, R2249 (1995).
[15] N. T. Son, O. Kordina, A. O. Konstantinov, W. M. Chen, E. Sörman, B. Monemar, and E. Janzén, Appl. Phys. Lett. **65**, 3209 (1994).
[16] N. T. Son, W. M. Chen, O. Kordina, A. O. Konstantinov, B. Monemar, E. Janzén, D. M. Hofman, D. Volm, M. Drechsler, and B. K. Meyer, Appl. Phys. Lett. **66**, 1074 (1994).
[17] G. Wellenhofer and U. Rössler, Phys. Status Solidi B **202**, 107 (1997).
[18] W. R. L. Lambrecht, S. Limpijumnong, S. N. Rashkeev, and B. Segall, Phys. Status Solidi B **202**, 5 (1997).
[19] H. Brooks, Phys. Rev. **83**, 879 (1951).
[20] M. Lundstorm, *Fundamentals of Carrier Transport*, *Modular Series on Solid State Devices* (Addison-Wesley, Reading, MA, 1990), Vol. X.
[21] B. K. Ridley, *Quantum Processes in Semiconductors*, 3rd ed. (Clarendon, Oxford, 1992).
[22] M. Cuevas, Phys. Rev. **164**, 1021 (1967).
[23] L. M. Falicov and M. Cuevas, Phys. Rev. **164**, 1025 (1967).
[24] K. M. Itoh, T. Kinoshita, W. Walukiewicz, J. W. Beeman, E. E. Haller, J. Muto, J. W. Farmer, and V. I. Ozhogin, Mater. Sci. Forum **258-263**, 77 (1997).
[25] J. Bardeen and W. Shockley, Phys. Rev. **80**, 72 (1950).
[26] H. Callen, Phys. Rev. **76**, 1394 (1949).
[27] D. K. Ferry, Phys. Rev. B **14**, 1605 (1976).
[28] G. Rutsch, R. P. Devaty, D. W. Langer, L. B. Rowland, and W. J. Choyke, Mater. Sci. Forum **264-268**, 517 (1998).
[29] S. Karmann, W. Suttrop, A. Schöner, M. Schadt, C. Haberstroh, F. Engelbrecht, R. Helbig, and G. Pensl, J. Appl. Phys. **72**, 5437 (1992).
[30] I. Y. Yanchev, B. G. Amaudov, and S. K. Evtimova, J. Phys. C **12**, L765 (1979).
[31] B. Pödör, Phys. Status Solidi **16**, K167 (1966).
[32] A. I. Anselm and B. M. Askerov, Fiz. Tverd. Tela **3**, 3672 (1961) [Sov. Phys.–Solid State **3**, 2665 (1962)].
[33] A. O. Evwaraye, S. R. Smith, W. C. Mitchel, and M. D. Roth, Appl. Phys. Lett. **68**, 3159 (1994).
[34] W. C. Mitchel, A. O. Evwaraye, S. R. Smith, and M. D. Roth, J. Electron. Mater. **26**, 113 (1997).